Measuring Integrin Conformational Change on the Cell Surface with Super-Resolution Microscopy

Travis I. Moore[1,2], **Jesse Aaron**[3], **Teng-Leong Chew**[3], and **Timothy A. Springer**[1,2,4,*]

[1]Department of Biological Chemistry and Molecular Pharmacology, Harvard Medical School, Boston, MA 02115, USA

[2]Program in Cellular and Molecular Medicine, Boston Children's Hospital, Boston, MA 02115, USA

[3]Advanced Imaging Center, Janelia Research Campus, Howard Hughes Medical Institute, Ashburn, VA 20147, USA

Summary

We use super-resolution interferometric photoactivation and localization microscopy (iPALM) and a constrained photoactivatable fluorescent protein integrin fusion to measure the displacement of the head of integrin lymphocyte function-associated 1 (LFA-1) resulting from integrin conformational change on the cell surface. We demonstrate that the distance of the LFA-1 head increases substantially between basal and ligand-engaged conformations, which can only be explained at the molecular level by integrin extension. We further demonstrate that one class of integrin antagonist maintains the bent conformation, while another antagonist class induces extension. Our molecular scale measurements on cell-surface LFA-1 are in excellent agreement with distances derived from crystallographic and electron microscopy structures of bent and extended integrins. Our distance measurements are also in excellent agreement with a previous model of LFA-1 bound to ICAM-1 derived from the orientation of LFA-1 on the cell surface measured using fluorescence polarization microscopy.

Graphical abstract

Using super-resolution interferometric photoactivation and localization microscopy (iPALM), Moore et al. measure the nanometer scale conformational change that occurs upon activation of the leukocyte integrin LFA-1 on the surface of migrating T cells. The authors also measure the effect of antagonists on integrin conformation.

---

*Correspondence: springer_lab@crystal.harvard.edu.
[4]Lead Contact

Declaration of Interests: The authors declare no competing interests.
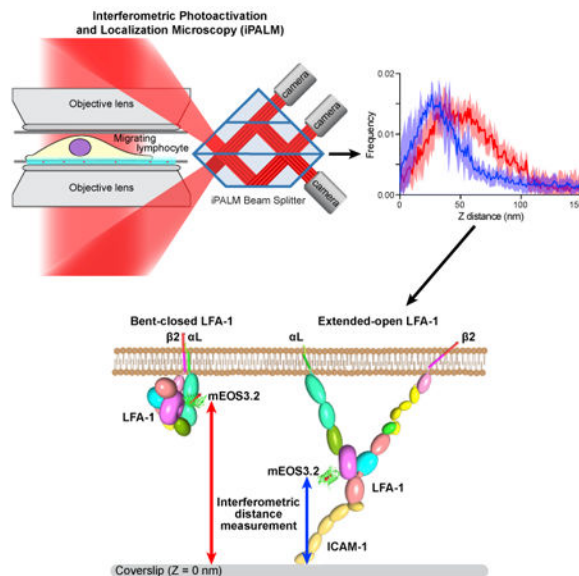
Introduction

Integrins are large multi-conformational surface receptors that mediate cell-cell and cell-extracellular matrix interactions (Hynes, 2002; Springer and Dustin, 2012). They function to mediate cell adhesion and cell migration through binding of their extracellular domain to ligand and their cytoplasmic domain to adaptor proteins that mediate linkage to the actin cytoskeleton. Lymphocyte function-associated 1 (LFA-1, integrin αLβ2), binds to intercellular adhesion molecules (ICAMs), a family of cell-surface molecules with tandem immunoglobulin-like superfamily domains. LFA-1 is important in almost all leukocyte functions that require cell-cell adhesion including antigen recognition, diapedesis, and migration within tissues.

Studies on purified integrins have revealed three conformational states (Figure 1A). In a bent-closed conformation, the integrin head and upper legs (the headpiece) interact over an extensive interface with the lower legs. In integrin extension, this interface is broken and the upper and lower legs straighten at the knees. In a second type of conformational change centered in the integrin βI domain, an internal or external ligand-binding site around a metal ion-dependent adhesion site (MIDAS) remodels, and pivoting (swing-out) of the hybrid domain occurs at its interface with the βI domain (Figure 1A). This change is known as headpiece opening or βI domain opening and converts the low-affinity, extended-closed conformation to the high-affinity, extended-open conformation (Springer and Dustin, 2012) (Figure 1A). Some integrins, including LFA-1, contain an αI domain that is inserted in the α-subunit β-propeller domain. The αI domain contains an internal ligand that binds to the open conformation of the βI domain, which relays allostery to the αI domain by converting the αI domain from the closed to the high-affinity, open conformation (Sen and Springer, 2016). Two classes of small molecules antagonize LFA-1 by different mechanisms (Shimaoka and Springer, 2003). αI allosteric antagonists bind to the αI domain and stabilize its closed conformation. α/βI allosteric antagonists bind to the internal ligand binding pocket

at the βI MIDAS near its interface with the α-subunit β-propeller domain, block allosteric communication between the αI domain and the remainder of the integrin, and stabilize the extended-open conformation in the absence of αI domain opening.

To date, no distance measurements on integrins on intact cells support conversion between the three states. Distance measurements on cell-surface integrins are important for many reasons. Although integrins are portrayed in cartoons with their legs normal to the membrane (Figure 1A), there is no evidence for this orientation. Linkers between the last domain in each integrin leg and the transmembrane domain are flexible, and even in the more constrained bent-closed conformation, marked tilting relative to the plasma membrane is possible (Zhu et al., 2013). Furthermore, force transmitted through integrins between extracellular ligands and the cytoskeleton may tilt them. Measurements of forces on integrins and their ligands (Chang et al., 2016; Nordenfelt et al., 2016; Sun et al., 2016) and thermodynamic measurements on integrins (Li and Springer, 2018) are consistent with a cytoskeletal force model of integrin activation. In this model, binding of adaptor proteins such as talin to the in-tegrin β-subunit cytoplasmic domain (Calderwood et al., 2013) enables actin to apply force to the integrin. If the integrin simultaneously binds an immobilized ligand that resists the cytoskeletal force, the tensile force transmitted through the integrin stabilizes the extended-open high-affinity state, and should align the integrin in the direction of actin retrograde flow. Constrained insertion of GFP into integrin heads, and measurement of the orientation of its fluorescence transition dipole confirmed this prediction, and also suggested that integrins were tilted by applied force (Nordenfelt et al., 2017; Swaminathan et al., 2017).

In this work, we setout to directly measure predicted changes in position of the head of LFA-1 relative to the plasma membrane. Such measurements have not previously been reported for surface molecules; however, we thought that the large predicted length scales of conformational change in integrins (Figure 1A) might make them accessible to super-resolution microscopy. Whereas optical microscopy accommodates whole cell imaging, it does not traditionally have the nm resolution needed to measure protein conformational change. With the advent of super-resolution microscopy, this barrier has been greatly reduced with points as close as 20 nm commonly resolved from one another (Betzig et al., 2006; Galbraith and Galbraith, 2011; Lambert and Waters, 2017; Patterson et al., 2010; Schermelleh et al., 2010). In particular, interferometric photoactivation and localization microscopy (iPALM) is well suited to measuring protein conformational change on the cell surface as it achieves <20 nm super-resolution not only laterally (XY), parallel to the cover-slip/substrate, but also has an axial resolution (Z) of <10 nm, perpendicular to the substrate and cell membrane (Case and Waterman, 2015; Kanchanawong et al., 2010; Shtengel et al., 2009, 2014). Here, we directly measure LFA-1 extension on the cell surface of migrating leukocytes using iPALM. We show distance changes that are dependent on binding to LFA-1's native ligand, ICAM-1, and that are modulated by allosteric antagonists. Our work shows that directly measuring conformational change of cell-surface proteins with multiple tandem modules in their extracellular domains is possible using optical microscopy techniques such as iPALM.

Results

Construction of Constrained mEos3.2-LFA-1 Fusion

To measure displacements of the head of LFA-1 between distinct integrin conformational states, photoswitchable mEos3.2 (Zhang et al., 2012) was inserted in the β-propeller domain of the αL-subunit of LFA-1 (Figure 1A). The insertion position creates no clashes with other domains in any LFA-1 conformational state and has been validated previously with cutinase and EGFP to have no effects on LFA-1 function (Bonasio et al., 2007; Nordenfelt et al., 2017). GFP and EosFP are homologous fluorescent proteins with a β-barrel domain with N and C termini at the same end of the β-barrel. We inserted mEos3.2 into a previously described EGFP-LFA-1 fusion in which flexible N- and C-terminal residues of the fluorescent protein were truncated and Gly residues in the integrin were mutated to Ala or Gln to increase constrainment (Experimental Procedures). Rosetta was used to model the orientation of the connections between the fluorescent protein and LFA-1. Ensembles showed a relatively narrow range of orientations (Nordenfelt et al., 2017). In the Discussion, we compare our experimental results to the position of the fluorophore in models of mEos3.2-LFA-1 in different conformational states.

Localization of the Head of LFA-1 in Migrating Cells Adherent to ICAM-1

Jurkat T-lymphocytes that stably expressed mEos3.2-LFA-1 were established through lenti-virus infection. To place iPALM measurements of integrin headpiece localization in context, cellular references were established. Stable lines of human Jurkat T-lymphocytes that expressed a plasma membrane marker (CAAX fused to mEos3.2) or actin cytoskeleton marker (LifeAct-mEos3.2) were established in parallel to the mEos3.2-LFA-1 Jurkat line. Cells were seeded on coverslips coated with ICAM-1 and allowed to migrate prior to fixation and iPALM imaging. Cells were imaged and each molecular emission localized in X, Y, and Z coordinates, with Z measured relative to the substrate surface bearing the integrin ligand (Figure 1B). Representative cells with molecular localizations colored according to Z position for LFA-1, CAAX, and LifeAct are shown in Figures 2A–2C, respectively. Distributions of Z positions measured in multiple cells were well fit to Gaussians (Figures 2D, 2E, S1, and S2). However, to avoid model bias, we report in the text below the average median values for Z localizations in individual cells ± SD (average Z median by cell, Table 1). These give a larger estimate of error than the Z median value for all cells, with the 95% confidence interval estimated by bootstrapping (Z median all cells, Table 1). Finally, we also report the Z centers of Gaussians for all localizations (Gaussian Z center, Table 1).

The measurements show that the peaks of the CAAX-mEos3.2 and LifeAct-mEos3.2 distributions localize 62.3 ± 1.4 and 95.3 ± 1.3 nm away from the coverslip, respectively. In contrast, the headpiece of the LFA-1-mEOS3.2 fusion localizes significantly closer to the coverslip at 36.1 ± 1.5 nm (Figures 2D and 2F; Table 1). Thus, the mEos3.2 fluorophore in the headpiece of LFA-1 on ICAM-1 substrates is 26.2 nm closer to the substrate than the fluorophore in CAAX-mEos3.2 (Table 2). In the Discussion, we estimate that the fluorophore in CAAX-mEos3.2 lies 7 nm below the outer face of the plasma membrane. Subtracting 7 nm from the 26.2 nm distance between LFA-1-mEOS3.2 and CAAX-

mEOS3.2 gives an estimate that the LFA-1 headpiece is ~19 nm above the lipid bilayer on the outside of the cell.

The divalent cation Mn^{2+} binds to integrin βI domains, stabilizes ligand binding, and makes them less dependent on activation by the actin cytoskeleton. In Mn^{2+}, the distance of LFA-1-mEos3.2 from the substrate-bearing coverslip was 32.0 ±1.9 nm and significantly closer than the distance of 36.1 ± 1.5 nm measured in Mg^{2+} (Figures 2E and 2F).

On Fibronectin Substrates, the LFA-1 Headpiece Is Markedly Closer to the Cell Surface

To obtain comparable measurements on LFA-1 when it is not engaged to ligand, we used fibronectin substrates. Jurkat cells express integrin α4β1 and utilize it to adhere and migrate on fibronectin substrates. To set the stage for LFA-1 measurements, we first determined positions of CAAX-mEos3.2 and LifeAct-mEos3.2 in Jurkat cells on fibronectin substrates and found values of 61.0 ± 1.8 and 95.6 ± 2.1 nm, respectively (Figures 3D and 3G). These values were very close to, and not significantly different from, measurements on ICAM-1 substrates (Figures S1A–S1D). Thus, the plasma membranes and actin cytoskeleton are similarly positioned in Jurkat cells on ICAM-1 and fibronectin substrates.

On fibronectin substrates, we expected LFA-1 to be in its bent conformation (Figures 1A and 1B). Indeed, we found that the fluorophore of LFA-1-mEos3.2 is 50.9 ± 2.9 nm away from the substrate on fibronectin substrates (Figures 3D and 3G) compared to 36.1 ± 1.5 nm on ICAM-1 substrates (Table 1). The distance between CAAX-mEos3.2 and LFA-1-mEos3.2 was 10.1 ± 3.4 nm on fibronectin compared to 26.2 ± 2.0 nm on ICAM-1 (Figures S1E and S1F; Table 2). Thus, the LFA-1 headpiece significantly extends 16.1 ± 3.9 nm axially further above the membrane when bound to ICAM-1 (difference from CAAX in Table 2 ± error-propagated SD).

LFA-1 Headpiece Position above the Plasma Membrane Is Perturbed by Small-Molecule Allosteric Modulators

As explained in the Introduction, α/βI and αI allosteric antagonists of LFA-1 inhibit ligand binding by two different mechanisms that stabilize extended and bent conformations, respectively. We studied these antagonists using cells on fibronectin substrates. Because LFA-1 does not bind ligand on fibronectin substrates, we were able to test effects of antagonists on LFA-1 conformation independent of any effect on ligand binding.

In 10 μM XVA143, the LFA-1-mEos3.2 fluorophore moved closer to the substrate (Figures 3E and 3G). The distribution of fluorescence also widened, perhaps because extended LFA-1 can adopt many different orientations relative to the cell surface normal. Compared to the resting state, XVA143 decreased the Z median distance from the coverslip from 50.9 ± 2.9 to 40.4 ± 2.0 nm (Table 1). BIRT377 is thought to stabilize the bent conformation and did not significantly change the distance of the headpiece from the coverslip with a Z median value of 53.3 ± 2.0 (Figures 3F and 3G; Table 1).

Discussion

Using iPALM, we have measured the distance of the LFA-1 head from the coverslip on adherent Jurkat cells. Measurements on cells adherent to ICAM-1 and fibronectin allowed us to examine how ligand binding and allosteric antagonists perturbed distances. Measurements of the distance of the actin cytoskeleton and mEos3.2 tethered to the intracellular face of the plasma membrane provided internal comparisons to LFA-1 and also showed that the distance from the coverslip of the Jurkat actin cytoskeleton and plasma membrane were similar on ICAM-1 and fibronectin substrates. Our measurements show that on ICAM-1 substrates, mEos3.2 attached to the LFA-1 head is significantly further away from the membrane than on fibronectin substrates, by 16.1 ± 3.9 nm. These specific measurements of receptor axial movement on the surface of a cell provide a large advance over previous FRET studies that have suggested that integrins underwent conformational change on cell surfaces, but did not provide distance measurements (Askari et al., 2010; Chigaev et al., 2015; Hyun et al., 2009; Kim et al., 2003; Larson et al., 2005). Integrin conformational change is well established for purified integrins and the use of conformation-specific Fabs both with purified proteins and with intact cells has clearly established that integrin conformational change to the extended-open conformation is required both for high-affinity ligand binding and for cellular adhesion to ligands on substrates (Chen et al., 2010; Li and Springer, 2017; Nishida et al., 2006; Su et al., 2016). We now provide measurements of integrin extension on cell surfaces that agree with previous correlations made with conformation-specific probes. The bent-closed integrin conformation can clearly bind ligand, although with ~1,000-fold lower affinity than the extended-open conformation. Findings that integrins can bind ligand in the absence of extension have been used to argue against the importance of extension in integrin function (Adair et al., 2013; Fan et al., 2016). However, the sine qua non of integrin function is mediation of cell adhesion and migration, and our measurements clearly establish that on migrating, adherent cells integrins are extended.

What can we infer from our measurements about integrin structure on intact cells, either in absolute distances relative to the plasma membrane, or in relative distances between integrin conformational states? Crystal structures of mEOS show that its β-barrel domain has dimensions of 4.5×2 nm and that its fluorophore locates close to center of the β-barrel (Protein Data Bank: 3S05). Prenylation of the CAAX moiety appended to the C terminus of mEos3.2 targets it to the inner face of the plasma membrane (Vincent et al., 2003). Moreover, mEos is basic with a predicted pI of 7.7 and is thus predicted to interact with the negatively charged inner face of the plasma membrane. The plasma membrane bilayer is 5 nm thick. We thus expect that the mEos3.2 fluorophore lies ~2 nm below the inner face and ~7 nm below the outer face of the plasma membrane. Structures of different integrin regions and conformations are known from crystallography, electron microscopy, solution X-ray scattering, nuclear magnetic resonance, and disulfide crosslinking restraints (Springer and Dustin, 2012). Hybrid methods were used to determine the structure of an integrin in the bent-closed conformation in intact cells. The latter revealed that flexible linker segments in each integrin subunit between the last leg domain and the transmembrane domain enable marked tilting of the bent-closed conformation relative to the plasma membrane (Zhu et al.,

2009). Therefore, while integrins are usually shown in cartoons with their lower leg domains normal to the plasma membrane, experimental evidence shows that tilting is possible. Measurements such as reported here are thus essential for understanding integrin orientation on cells. To build appropriate cell-surface models of LFA-1, we use crystal structures of LFA-1 and the closely related β2 integrin αxβ2 and electron microscopy (EM) projection averages showing LFA-1 and αxβ2 in the bent-closed, extended-closed, and extended-open conformations. Rosetta ensembles revealed a relatively narrow range of orientations between the fluorescent protein and the LFA-1 β-propeller domain.

Using the average orientation of mEos3.2 relative to the integrin, we measured fluorophore distance from the extracellular surface of the plasma membrane in different LFA-1 conformational states (Figure 4). The fluorophore-membrane distance in the bent-closed conformation was 4 nm; tilting to the limits of ectodomain contact with the plasma membrane of up to 40° resulted in distances of 3.5 to 4 nm. These distances in structural models are comparable to our experimental integrin-CAAX distances with 7 nm subtracted for resting LFA-1 and LFA-1 in presence of BIRT377 on fibronectin substrates of 3.1 ± 3.4 and 0.7 ± 2.7 nm, respectively. The distances from bent-closed integrin crystal structures and from iPALM measurements on cells are within 1 to 3 nm of one another, and are thus in excellent agreement. It is unlikely that extended conformations make contributions to these measurements. Integrin α5β1 is >99.8% in the bent closed conformation on the cell surface (Li etal., 2017). Stabilizing extension increases affinity of cell-surface LFA-1 by ~1,000-fold, also suggesting that ~99.9% of LFA-1 is constitutively in the bent closed conformation (Schurpf and Springer, 2011).

Extended integrins show multiple, flexible domain-domain junctions. Using models of the extended-closed and extended-open conformations built using crystallographic and EM structures, we estimated a maximum distance of the fluorophore from the membrane of 20.7 nm; the minimum distance might only be limited by mEos3.2 collision with the plasma membrane at ~2 nm. The extended-open conformation stabilized by XVA143 on fibronectin substrates had a median fluorophore distance from the membrane of 13.6 ± 2.7 nm, within the estimated range of 2 to 20.7 nm. The relatively broad distribution of fluorophore distances measured here in presence of XVA143 is also consistent with integrin inter-domain flexibility and especially with the ability of the ectodomain to tilt with respect to the plasma membrane.

When simultaneously bound to ICAM-1 and the actin cyto-skeleton, the orientation of the extended-open conformation of LFA-1 will be constrained by the tensile force transmitted through LFA-1 that provides the traction for cell migration. We previously measured the orientation of the fluorescent transition dipole of a constrained GFPfusion that was inserted in the integrin head very similarly to the mEos3.2 fusion used here (Nordenfelt et al., 2017). These dipole orientation measurements provided evidence that the axis of force transmission within LFA-1 aligns with the direction of actin retrograde flow and also suggested that LFA-1 was tilted relative to the membrane normal by $45° \pm 25°$. At 45°, the extended-open conformation has a fluorophore-membrane distance of 19.2 nm (Figure 4). At tilts relative to the membrane normal of 70° and 40° the distances were 9.6 and 20.7 nm, respectively. These results based on structural models are very similar to our iPALM estimate of the

fluorophore-membrane distance of 19.2 ± 2.0 nm. The error of ± 2.0 nm is propagated from the distance measurement errors on LFA-1-mEOS3.2 and CAAX-mEos3.2 fusions. This error does not include an error for our estimate of the distance between the CAAX-mEos3.2 fluorophore and the membrane, but we expect that this estimate is off by no more than 1 nm. A caveat is that on ICAM-1 substrates, we do not know what proportion of the LFA-1 is (1) bound to ICAM-1 and in the tilted extended-open conformation described above, and (2) unbound and thus predominantly in the bent-closed conformation. Addition of Mn^{2+}, which activates integrins independently of the actin cytoskeleton, significantly increased the fluorophore-membrane distance on ICAM-1 substrates to 23.3 ± 2.3 nm (Table 2). This is consistent either with an increase in the population of the ligand-bound extended-open conformation, or with a decrease in tilt relative the membrane normal expected from the ability of Mn^{2+} to render cell adhesion independent of force application by the cytoskeleton. We did not expect a large effect of Mn^{2+}, because the LFA-1 is already physiologically activated by the tensile force transmitted through it between ICAM-1 bound to the substrate and the LFA-1 β-subunit cytoplasmic domain linked through adaptors to actin cytoskeleton retrograde flow (Li and Springer, 2018; Nordenfelt et al., 2016, 2017). It is possible that the proportions of bent-closed and extended-open integrins differ in different regions of a migrating cell, such as in the lamellipodium, cell body, and uro-pod. However, considering the large overlaps in integrin distance distributions on fibronectin and ICAM-1 substrates and the good fit of our data to a single Gaussian, discerning such differences in proportions of conformational states on the surface of migrating cells would be challenging.

Overall, our iPALM measurements of positions of the mEos3.2 fluorophore attached to the head of LFA-1 relative to the mEos3.2 fluorophore attached to the inner surface of the plasma membrane are in excellent agreement with the distances expected based on structures of integrins in bent-closed and extended-open conformations (Figure 4). The integrin head is 16.1 ± 3.9 nm further above the membrane when physiologically engaged to ligand on ICAM-1 substrates than when non-engaged on fibronectin substrates. The agreement between the distance measurements on atomic structures and on cells (Figure 4) strongly supports the relevance of integrin extension to integrin function in cell adhesion and migration.

Our studies not only represent a step forward in solidifying a model for integrin activation, a major class of cell adhesion receptors, but also demonstrate that it is possible to use optical microscopy techniques to directly measure protein conformation at the molecular scale. Our method could be applied to other receptors with multiple tandem domain modules in their extracellular domains, including cytokine receptors and viral fusion proteins. Super-resolution microcopy lends itself to preserving cellular architecture with whole cell-friendly preparations while interrogating conformational statesonthe cell surface. While our studies utilized the unusually large scale of conformational change in integrins, with continued advancements in fluorescent protein design and protein-fluorophoreconjugationthesetechniquesshouldbeavail-able to a widening number of cell-surface proteins.

Experimental Procedures

Plasmids

mEos3.2-LifeAct-7 from Michael Davidson (Riedl et al., 2008) (Addgene plasmid #54696), was used to amplify mEos3.2 for construction of fusions with LFA-1 and CAAX-sequences. mEOS3.2-CAAX was constructed by attaching an 8 amino acid linker, PAGCMSCK, and CaaX sequence from HRas, CVLS, to the C terminus of mEos3.2 (Vincent et al., 2003). To construct the constrained LFA-1-mEos3.2 fusion, we began with the αL-T fusion described in (Nordenfelt et al., 2017). In αL-T, five residues were removed from the N terminus and one residue from the C terminus of moxGFP and it was inserted into the β3-β4 loop of blade 4 of the αL integrin β-propeller domain between the LLFQEPQG and GGHNSQ sequence in this loop. Adjacent to the insertion, the αL QG and GG sequences were mutated to QA and AQ, respectively, to make them less flexible. Residues M8-A216 of mEOS3.2 were used to replace V12-A227 of moxEGFP (Costantini et al., 2015) within αL-T. The LFA-1-mEos3.2 plasmid was constructed by overlap PCR (Phusion High-Fidelity DNA Polymerase, New England Biolabs) to combine three segments (A: αL-moxGFP-NTerm; B: moxGFP-NTerm-mEOS3.2-moxGFP-CTerm; C: moxGFP-CTerm-αL). The complete A–C fusion sequence and wild-type αL-pcDNA3.1 plasmids were cut with restriction enzymes (New England Biolabs) and ligated using T4 ligase (New England Biolabs) after dephosphorylation (rAPID alkaline phosphatase, Roche) and purification (QIAGEN). Plasmids were verified with size matching of multi-site single restriction enzyme digestion, inserts were verified by full sequencing and surface expression validated by transient co-expression with β2 in HEK293T cells. Primers used were: A1: 5′-AGA TGT GGT TCT AGA GCC ACC ATG AAG GAT CCT GC-3′; A2: 5′-CAC CCC GGT GAA CAG CTC CTC GGC CTG TGG CTC TTG GAA CAG CAG-3′; B1: 5′- GCC GAG GAG CTG TTC ACC GGG GTG ATG AAG ATC AAA CTC CGT ATG GAA G –3′; B2: 5′- TAC AGC TCG TCC ATG CCG TGA GTG ATC CCA GCA ACA GCA TGC TCA TAC AGC TT-3′; C1: 5′- GAT CAC TCA CGG CAT GGA CGA GCT GTA CGC ACA ACA CTG GAG CCA GGT CCA GAC-3′; and C2: 5′- ACT CTT AGT AGC GGC CGC TCA GTC CTT GCC ACC ACC-3′.

Lentiviral Transfection, Cell Culture, and Experimental Treatments

JurkatTcells (clone E6.1) were cultured in RPM1-1640 medium with 10% FBS (Sigma) in 5% CO_2. The Gateway system from Thermo Fisher was used to create lentiviral constructs of mEos3.2 fusions of LFA-1, CAAX, and LifeAct. Constructs were inserted into the pLX302 lentivirus plasmid. 293T cells cultured in DMEM supplemented with 10% FBS were co-transfected with the lentiviral plasmid, psPAX2 and CMV-VSV-G using Lipofectamine 2000 (Thermo Fisher) to produce virus. Virus in supernatants was concentrated using Lenti-X (Clontech) and Jurkat cells transduced and selected using 3 μg/mL puromycin (pLX302). Gold nanoparticles (80–100 nm) were absorbed to cover-slips at a density of ~2000 per mm^2 and immobilized by 30–50 nm of sputter-coated SiO_2, as previously described. These gold nanoparticles acted as fluorescent fiducial markers for calibration, image alignment and correction. Prior to experiments, coverslips were cleaned with 1 M KOH, washed with Dulbecco's phosphate-buffered saline (DPBS, Thermo Fisher), adsorbed overnight at 4°C with 10 μg/mL Ni-NTA agarose purified soluble ICAM-1-His6

(D1–D5) (Schurpf and Springer, 2011) or 10 μg/mL fibronectin (Thermo Fisher) in DPBS, blocked with 1% BSA in L-15 medium at 37°Cfor60 min, and washed with L-15 medium (Thermo Fisher). Cells were suspended in incubation medium (L-15 medium supplemented with 2 mg/mL glucose and 100 ng/mL SDF1-α, R&D Systems), added to fibronectin or ICAM-1 substrates, and incubated at 37°C for 60 min. For all cells migrating on fibronectin substrates, an equal volume of incubation medium containing 2× the final concentration of drug treatment or control was then added and cells incubated at 37°C for an additional 60 mins. Cells were treated with final concentrations of 10 μM XVA143(0.1% DMSO), 20 μM BIRT377 (0.04% DMSO), or 0.1% DMSO alone as a control. For all cells migrating on ICAM-1 substrates, an equal volume of incubation medium or incubation medium supplemented with 2× the final concentration of 1 mM Mn^{2+} was added, and cells were incubated a further 60 mins. All media ± treatments were prewarmed to 37°C. Cells were fixed with 10% paraformaldehyde and 1% glutaraldehyde in PHEM buffer (60 mM PIPES, 25 mM HEPES, 10 mM EGTA, 2 mM $MgCl_2$, pH 6.9) for 15 min and washed and stored in DPBS for imaging.

Image Collection and Analysis

The iPALM instrumentation has been previously described (Shtengel et al., 2014). The sample was mounted between two opposing 60× TIRF objectives (Nikon CFI Apochromat TIRF 60×, NA = 1.49, Nikon Instruments) with index matching immersion oil (Cargille type DF, Cargille Laboratories). mEOS3.2 single fluorophore activation was achieved with a neutral density filter actuated 50 mW 405 diode laser (Coherent), and fluorophore excitation with 150 mW 561 nm diode pumped solid-state laser (CrystaLaser). Both activation and excitation beams were focused through custom turning mirrors and adjusted radially to produce TIRF illumination. Emission signals collected by the two objective lenses were directed into the custom-designed 3-way beam splitter (Rocky Mountain Instruments) and output focused on three EMCCD cameras (Andor iXon DU-897, Andor Technology). iPALM image acquisition typically consisted of 25,000–50,000 images collected on the three Andor iXon EMCCD cameras operated in EM gain, frame-transfer mode with a 50-ms exposure per image. Instrument control and data acquisition were facilitated by custom software written in LABVIEW (National Instruments). Data analysis, image processing, and rendering were performed using custom software written in IDL (ITT Visual Information Solutions) and run on a Linux computational cluster at HHMI Janelia Farm Research Campus.

Image field of views were selected that had a minimum of 3 gold nanoparticle, fiducial markers for interferometry calibration, image alignment, and drift correction. The focal plane and lateral alignment of the two objectives were adjusted for each image set using a single fiducial, which was subsequently used to further align the optics and beam splitter for optimal interference by oscillating the sample in the axial direction over 250 nm. Once alignment and the interferometric effect were archived, a calibration dataset was collected by translating the sample/fiducial over an axial range of 1,000 nm in 10 nm steps, causing the intensity of the fiducial's emission to oscillate proportionally but in different phases between the three EMCCD cameras.

Raw datasets from the three cameras were processed to localize individual molecules in X, Y, and Z as previously described (Kanchanawong et al., 2010; Shtengel et al., 2014). Images from each individual camera were aligned and summed, with individual emissions fitted to a two-dimensional Gaussian by nonlinear least-squares fitting resulting in X, Y coordinates for each fluorescent particle. The Z position of each fluorescent molecule was determined from the calibration curve collected at the time of image acquisition. Sample drift in X, Y, and Z were corrected by tracking the positions of the fiducial markers.

Datasets were analyzed over the entirety of individual cells, excluding regions with fiducial markers. X, Y, and Z coordinates of mEOS3.2 fluorescent localizations were then extracted. The mean Z position of auto fluorescence emanating from the cover glass around each cell was determined, fit to a Gaussian, and the Z center of coverslip autofluorescence was subtracted from mEOS3.2 Z values for each cell to set the axial position of the cover glass to 0 nm (Kanchanawong et al., 2010). Axial positions of fluorescent molecules were plotted in 1-nm binned histograms. We report histograms for combined data from all cells with 95% confidence intervals calculated using the bootstrapping method, where datasets were resampled 10,000 times. The combined data were used to calculate Z medians with 95% confidence interval from bootstrapping. The 95% confidence intervals at all points in the Z localization distributions are also shown in plots in Figures 2 and 3. The Z median for individual cells was determined and the mean and SD between cells reported. We also fit all localizations to a Gaussian and report goodness-of-fit (R^2). Furthermore, we fit data for each cell to Gaussians, and report the average Gaussian Z center and SD. Results are summarized in Table 1. Conditions were compared for statistical difference using a two-tailed Mann-Whitney test, with differences determined to be significant when $p < 0.05$.

To estimate the distance of the LFA-1 fluorophore from the membrane, the mean Z median of each condition was compared to the mean Z median of mEOS3.2-CAAX on the corresponding substrate. As mEos3.2-CAAX is attached to the inner leaflet of the cellular membrane, the distance estimate was corrected by subtracting membrane thickness (5 nm) and an estimate in the Discussion of average distance of the mEOS3.2-CAAX fluorophore from the membrane (2 nm).

Statistical Analysis

Differences between iPALM Z median were determined by two-tailed Mann-Whitney to compare results among conditions and individual cells and differences considered significant at $p < 0.05$. All data are presented as mean ± 1 SD of the mean, unless otherwise stated. 8–13 cells were assessed from 2 independent sample preparations per condition. Detailed information on replication of experiments can be found in the figure legends and Table 1.

Determining mEOS3.2 Orientation and Fluorophore Distance from the Membrane in Models of mEOS3.2-LFA-1

Estimates of the distance between the membrane and the fluorophore of mEOS2.3 were determined using models of the bent and extended conformations of LFA-1. LFA-1 models were hybrids of LFA-1 ($\alpha_L\beta_2$) and the closely related integrin $\alpha_X\beta_2$. PyMol (Schrodinger) was used to build models and to create figures. A bent-closed model was built by

superimposing the β-propeller domain from an $\alpha_L\beta_2$ headpiece crystal structure (Sen and Springer, 2016) onto bent-closed $\alpha_X\beta_2$ chains A and B from the protein data bank (PDB): 5ES4. TM domains were added from model 5 of intact integrin $\alpha_{IIb}\beta_3$ (Zhu et al., 2009). The model was superimposed into a Cartesian coordinate system in which the membrane bilayer is in an XY plane, which allowed measuring distance to the membrane directly as the Z coordinate of atomic XYZ coordinates. For the extended-closed model, the headpiece portion of the bent-closed conformation was rotated 150° about an axis between headpiece residues A751–A752 and B460–B461, that separate the headpiece from the lower legs. For the extended-open model, the open head of PDB: 2VDR was superimposed onto the head of the extended-closed LFA-1 model, and superimposition on the PDB: 2VDR hybrid domain was used to obtain an open conformation of the LFA-1 model hybrid domain and more C-terminal domains. Superimposition of the head of PDB: 4NEH was used to obtain its αI domain orientation, and then a structure of the LFA-1 αI domain bound to ICAM domains 1 and 2 (D1D2, PDB: 1MQ8) was superimposed on the αI domain from PDB: 4NEH to incorporate the αI domain bound to ICAM domains 1 and 2 in the model. The structure of a D1D4 fragment of ICAM-5 (PDB: 4OIB) was superimposed, and a monomeric structure of D3D5 (PDB: 2OZ4) was superimposed to obtain a D1D5 ICAM model. The flexible inter-domain orientations of D1D5 were modified to obtain a more elongated conformation that would be obtained in presence of tensile force. The extended-open model was then rotated to tilt its head relative to the z axis at a 45° angle with respect to a previously defined coordinate system to match an orientation previously found for LFA-1 engaged with ICAM-1 and the actin cytoskeleton (Nordenfelt et al., 2017). For PyMol cartoon representations in Figures 1 and 4, the orientation of mEOS3.2 in bent-closed, extended-closed, and extended-open models was obtained by superimposition of a model near the centroid of the ensemble of GFP-LFA-1 orientations from Rosetta simulation of α_L-GFP-T (Nordenfelt et al., 2017). Finally, for the extended-closed model, the lower legs were separated by 20° by separate rotations of 10° of each lower leg. For the extended-open model, the ectodomain was rotated by 20° about an axis through the junction between the ectodomain and transmembrane portions of the α and β-subunits to obtain an orientation more parallel to the z axis.

The fusion junctions described under Plasmids resulted in a C-terminal fusion junction between the αL subunit and mEOS3.2 that was one residue shorter than in αL-T(L3) and one residue longer than in L2, which have similarly constrained and similar moxEGFP-LFA-1 orientations (Figure S8 in Nordenfelt et al., 2017). The N-terminal fusion junctions were identical in all three constructs; furthermore, the non-β-barrel C and N-terminal portions of moxEGFP-LFA-1, which influence orientation, were identical in moxEGFP-LFA-1 and mEOS3.2-LFA-1. Therefore, we used previous L2 and L3 moxEGFP-LFA-1 Rosetta simulations to estimate the position of the structurally homologous β-barrel domain in mEOS3.2-LFA-1. The centroid position of the fluorophore in mEOS3.2-LFA-1 was taken as midway between the centroids of the ensemble of GFP-LFA-1 orientations from Rosetta simulations of α_L-GFP-T (L3) and L2 (Nordenfelt et al., 2017). This centroid position is within 0.35 nm of L3 and L2 centroid positions and represents a reasonable approximation because 0.35 nm is only 10%–17% of the SD in estimates of height above the membrane

based on experimental measurements of mEOS3.2-LFA-1 fluorophore and mEOS3.2-CAAX fluorophore Z positions in this manuscript.

Supplementary Material

Refer to Web version on PubMed Central for supplementary material.

Acknowledgments

References

Adair BD, Xiong JP, Alonso JL, Hyman BT, Arnaout MA. EM structure of the ectodomain of integrin CD11b/CD18 and localization of its ligand-binding site relative to the plasma membrane. PLoS ONE. 2013; 8:e57951. [PubMed: 23469114]

Askari JA, Tynan CJ, Webb SE, Martin-Fernandez ML, Ballestrem C, Humphries MJ. Focal adhesions are sites of integrin extension. J Cell Biol. 2010; 188:891–903. [PubMed: 20231384]

Betzig E, Patterson GH, Sougrat R, Lindwasser OW, Olenych S, Bonifacino JS, Davidson MW, Lippincott-Schwartz J, Hess HF. Imaging intracellular fluorescent proteins at nanometer resolution. Science. 2006; 313:1642–1645. [PubMed: 16902090]

Bonasio R, Carman CV, Kim E, Sage PT, Love KR, Mempel TR, Springer TA, von Andrian UH. Specific and covalent labeling of a membrane protein with organic fluorochromes and quantum dots. Proc Natl Acad Sci USA. 2007; 104:14753–14758. [PubMed: 17785425]

Calderwood DA, Campbell ID, Critchley DR. Talins and kindlins: partners in integrin-mediated adhesion. Nat Rev Mol Cell Biol. 2013; 14:503–517. [PubMed: 23860236]

Case LB, Waterman CM. Integration of actin dynamics and cell adhesion by a three-dimensional, mechanosensitive molecular clutch. Nat Cell Biol. 2015; 17:955–963. [PubMed: 26121555]

Chang AC, Mekhdjian AH, Morimatsu M, Denisin AK, Pruitt BL, Dunn AR. Single molecule force measurements in living cells reveal a minimally tensioned integrin state. ACS Nano. 2016; 10:10745–10752. [PubMed: 27779848]

Chen X, Xie C, Nishida N, Li Z, Walz T, Springer TA. Requirement of open headpiece conformation for activation of leukocyte integrin alphaXbeta2. Proc Natl Acad Sci USA. 2010; 107:14727–14732. [PubMed: 20679211]

Chigaev A, Smagley Y, Haynes MK, Ursu O, Bologa CG, Halip L, Oprea T, Waller A, Carter MB, Zhang Y, et al. FRET detection of lymphocyte function-associated antigen-1 conformational extension. Mol Biol Cell. 2015; 26:43–54. [PubMed: 25378583]

Costantini LM, Baloban M, Markwardt ML, Rizzo M, Guo F, Verkhusha VV, Snapp EL. A palette of fluorescent proteins optimized for diverse cellular environments. Nat Commun. 2015; 6:7670. [PubMed: 26158227]

Fan Z, McArdle S, Marki A, Mikulski Z, Gutierrez E, Engelhardt B, Deutsch U, Ginsberg M, Groisman A, Ley K. Neutrophil recruitment limited by high-affinity bent β2 integrin binding ligand in cis. Nat Com-mun. 2016; 7:12658.

Galbraith CG, Galbraith JA. Super-resolution microscopy at a glance. J Cell Sci. 2011; 124:1607–1611. [PubMed: 21536831]

Hynes RO. Integrins: bidirectional, allosteric signaling machines. Cell. 2002; 110:673–687. [PubMed: 12297042]

Hyun YM, Chung HL, McGrath JL, Waugh RE, Kim M. Activated integrin VLA-4 localizes to the lamellipodia and mediates T cell migration on VCAM-1. J Immunol. 2009; 183:359–369. [PubMed: 19542447]

Kanchanawong P, Shtengel G, Pasapera AM, Ramko EB, Davidson MW, Hess HF, Waterman CM. Nanoscale architecture of integrin-based cell adhesions. Nature. 2010; 468:580–584. [PubMed: 21107430]

Kim M, Carman CV, Springer TA. Bidirectional transmembrane signaling by cytoplasmic domain separation in integrins. Science. 2003; 301:1720–1725. [PubMed: 14500982]

Lambert TJ, Waters JC. Navigating challenges in the application of superresolution microscopy. J Cell Biol. 2017; 216:53–63. [PubMed: 27920217]

Larson RS, Davis T, Bologa C, Semenuk G, Vijayan S, Li Y, Oprea T, Chigaev A, Buranda T, Wagner CR, Sklar LA. Dissociation of I domain and global conformational changes in LFA-1: refinement of small molecule-I domain structure-activity relationships. Biochemistry. 2005; 44:4322–4331. [PubMed: 15766261]

Li J, Springer TA. Integrin extension enables ultrasensitive regulation by cytoskeletal force. Proc Natl Acad Sci USA. 2017; 114:4685–4690. [PubMed: 28416675]

Li J, Springer TA. Energy landscapes differences among integrins establish the framework for understanding activation. J Cell Biol. 2018; 217:397–412. [PubMed: 29122968]

Li J, Su Y, Xia W, Qin Y, Humphries MJ, Vestweber D, Cabañas C, Lu C, Springer TA. Conformational equilibria and intrinsic affinities define integrin activation. EMBO J. 2017; 36:629–645. [PubMed: 28122868]

Nishida N, Xie C, Shimaoka M, Cheng Y, Walz T, Springer TA. Activation of leukocyte $\beta2$ integrins by conversion from bent to extended conformations. Immunity. 2006; 25:583–594. [PubMed: 17045822]

Nordenfelt P, Elliott HL, Springer TA. Coordinated integrin activation by actin-dependent force during T-cell migration. Nat Commun. 2016; 7:13119. [PubMed: 27721490]

Nordenfelt P, Moore TI, Mehta SB, Kalappurakkal JM, Swaminathan V, Koga N, Lambert TJ, Baker D, Waters JC, Oldenbourg R, et al. Direction of actin flow dictates integrin LFA-1 orientation during leukocyte migration. Nat Commun. 2017; 8:2047. [PubMed: 29229906]

Patterson G, Davidson M, Manley S, Lippincott-Schwartz J. Superresolution imaging using single-molecule localization. Annu Rev Phys Chem. 2010; 61:345–367. [PubMed: 20055680]

Riedl J, Crevenna AH, Kessenbrock K, Yu JH, Neukirchen D, Bista M, Bradke F, Jenne D, Holak TA, Werb Z, et al. Lifeact: a versatile marker to visualize F-actin. Nat Methods. 2008; 5:605–607. [PubMed: 18536722]

Schermelleh L, Heintzmann R, Leonhardt H. A guide to super-resolution fluorescence microscopy. J Cell Biol. 2010; 190:165–175. [PubMed: 20643879]

Schürpf T, Springer TA. Regulation of integrin affinity on cell surfaces. EMBO J. 2011; 30:4712–4727. [PubMed: 21946563]

Sen M, Springer TA. Leukocyte integrin $\alpha L\beta2$ headpiece structures: The αI domain, the pocket for the internal ligand, and concerted movements of its loops. Proc Natl Acad Sci USA. 2016; 113:2940–2945. [PubMed: 26936951]

Shimaoka M, Springer TA. Therapeutic antagonists and confor-mational regulation of integrin function. Nat Rev Drug Discov. 2003; 2:703–716. [PubMed: 12951577]

Shtengel G, Galbraith JA, Galbraith CG, Lippincott-Schwartz J, Gillette JM, Manley S, Sougrat R, Waterman CM, Kanchanawong P, Davidson MW, et al. Interferometric fluorescent super-resolution microscopy resolves 3D cellular ultrastructure. Proc Natl Acad Sci USA. 2009; 106:3125–3130. [PubMed: 19202073]

Shtengel G, Wang Y, Zhang Z, Goh WI, Hess HF, Kanchanawong P. Imaging cellular ultrastructure by PALM, iPALM, and correlative iPALM-EM. Methods Cell Biol. 2014; 123:273–294. [PubMed: 24974033]

Springer TA, Dustin ML. Integrin inside-out signaling and the immunological synapse. Curr Opin Cell Biol. 2012; 24:107–115. [PubMed: 22129583]

Su Y, Xia W, Li J, Walz T, Humphries MJ, Vestweber D, Cabañas C, Lu C, Springer TA. Relating conformation to function in integrin $\alpha5\beta1$. Proc Natl Acad Sci USA. 2016; 113:E3872–E3881. [PubMed: 27317747]

Sun Z, Guo SS, Fässler R. Integrin-mediated mechanotransduction. J Cell Biol. 2016; 215:445–456. [PubMed: 27872252]

Swaminathan V, Kalappurakkal JM, Mehta SB, Nordenfelt P, Moore TI, Koga N, Baker DA, Oldenbourg R, Tani T, Mayor S, et al. Actin retrograde flow actively aligns and orients ligand-engaged integrins in focal adhesions. Proc Natl Acad Sci USA. 2017; 114:10648–10653. [PubMed: 29073038]

Vincent S, Thomas A, Brasher B, Benson JD. Targetingof proteins to membranes through hedgehog auto-processing. Nat Biotechnol. 2003; 21:936–940. [PubMed: 12858181]

Zhang M, Chang H, Zhang Y, Yu J, Wu L, Ji W, Chen J, Liu B, Lu J, Liu Y, et al. Rational design of true monomeric and bright photoactivatable fluorescent proteins. Nat Methods. 2012; 9:727–729. [PubMed: 22581370]

Zhu J, Luo BH, Barth P, Schonbrun J, Baker D, Springer TA. The structure of a receptor with two associating transmembrane domains on the cell surface: integrin alphaIIbbeta3. Mol Cell. 2009; 34:234–249. [PubMed: 19394300]

Zhu J, Zhu J, Springer TA. Complete integrin headpiece opening in eight steps. J Cell Biol. 2013; 201:1053–1068. [PubMed: 23798730]

Highlights

- Integrin conformation can be measured using superresolution microscopy

- LFA-1 extends from membrane 16 nm between basal and ligand-engaged conformations

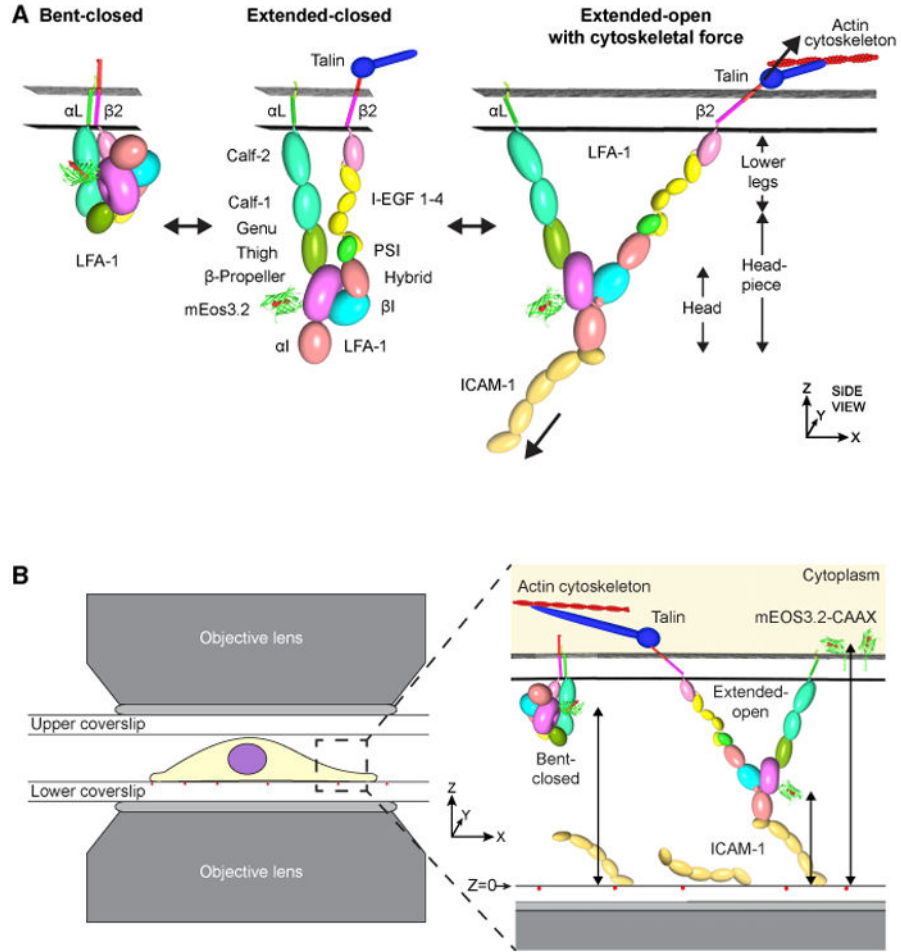- LFA-1 antagonists BIRT377 and XVA143 stabilize bent and extended conformations

Figure 1. Integrin Conformational States and iPALM

(A) Three conformational states of integrins (Springer and Dustin, 2012) and the cytoskeletal model of integrin activation. Ellipsoids or ribbon cartoons depict each integrin domain and mEos3.2 with its transition dipole (red double-headed arrows).

(B) Left: schematic of sample setup for iPALM imaging of migratory Jurkat T-lymphocytes adhered to ICAM-1 or fibronectin coated lower coverslips, with gold nanorod fiducial markers (orange spheres). Right: zoomed inset of the cell membrane, lower coverslip, and extracellular space. Extracellular regions and membrane bilayer thickness are to scale while talin is longer than shown and distance of actin from the plasma membrane is further than shown. The axial distances that are measured here between the lower coverslip (Z = 0) and the fluorophore (red) of mEOS3.2 (green) are shown with double-headed arrows.
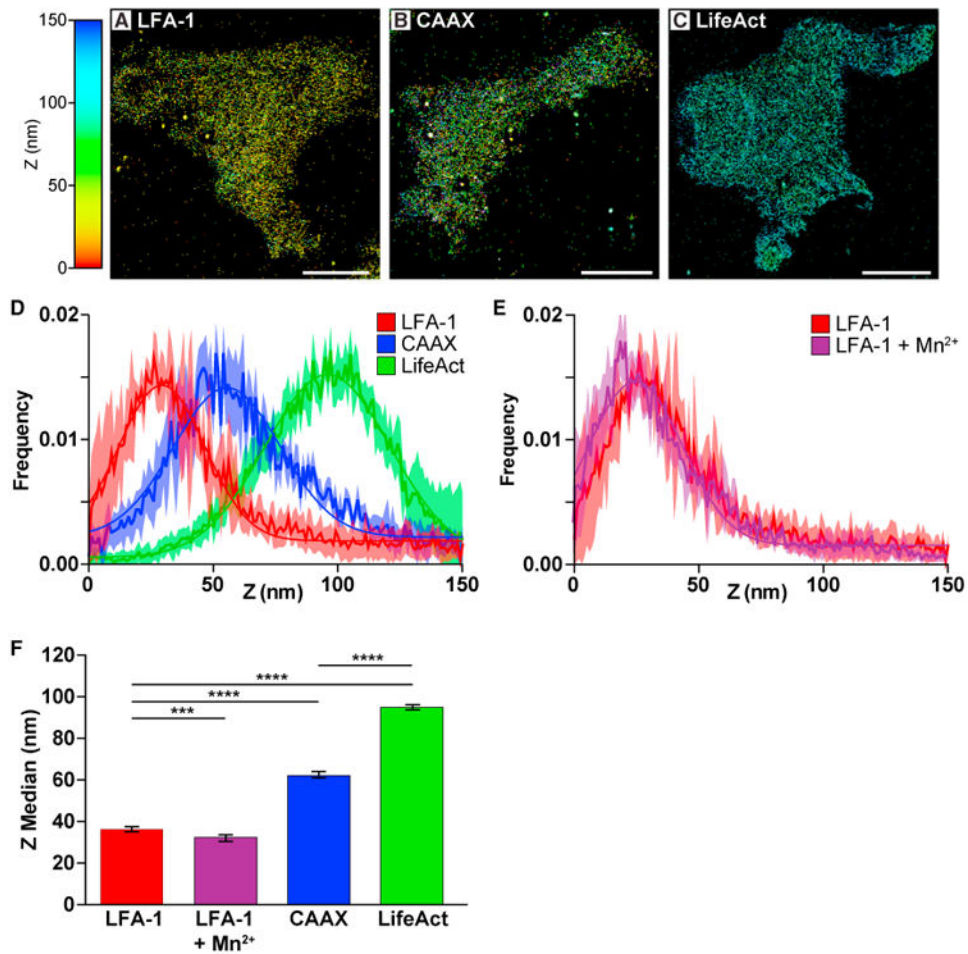
Figure 2. Fluorophore-Coverslip Distances Measured in Cells Migrating on ICAM-1

(A–C) Representative iPALM renderings of Jurkat cells expressing mEOS3.2-LFA-1 fusion (A), mEOS3.2-CAAX (B), or LifeAct-mEos3.2to label actin (C) migrating on substrates coated with 10 µg/mL ICAM-1. Single-molecule iPALM localizations are color-coded by Z position as shown in scale on left. Larger dots correspond to fiducial markers. Scale bars, 5 µm.

(D and E) Frequency histograms, with 1 nm bins, of axially localized mEOS3.2 emissions relative to the coverslip (Z = 0) in Jurkat cells migrating on coverslips coated with 10 µg/mL ICAM-1. Data are for the sum of measurements over N cells expressing mEOS3.2-LFA-1 in 1 mM Mg^{2+} (red, n = 12), 1 mM Mn^{2+} (purple, n = 9), CAAX-mEOS3.2 (blue, n=13) or LifeAct-mEOS3.2 (green, n = 10). Plots show the frequency(thickline) with 95% bootstrapped confidence interval (shaded region) and Gaussian fit (thin line) of the frequency for each construct.

(F) Mean Z median ± SD among n individual cells of mEOS3.2 emission axial localizations for Jurkat cells migrating on coverslips coated with 10 µg/mL ICAM-1. Two-tailed Mann-Whitney tests that compared results among n individual cells enumerated in (D) and (E) gave p values coded as ***$p < 0.001$ and ****$p < 0.0001$.
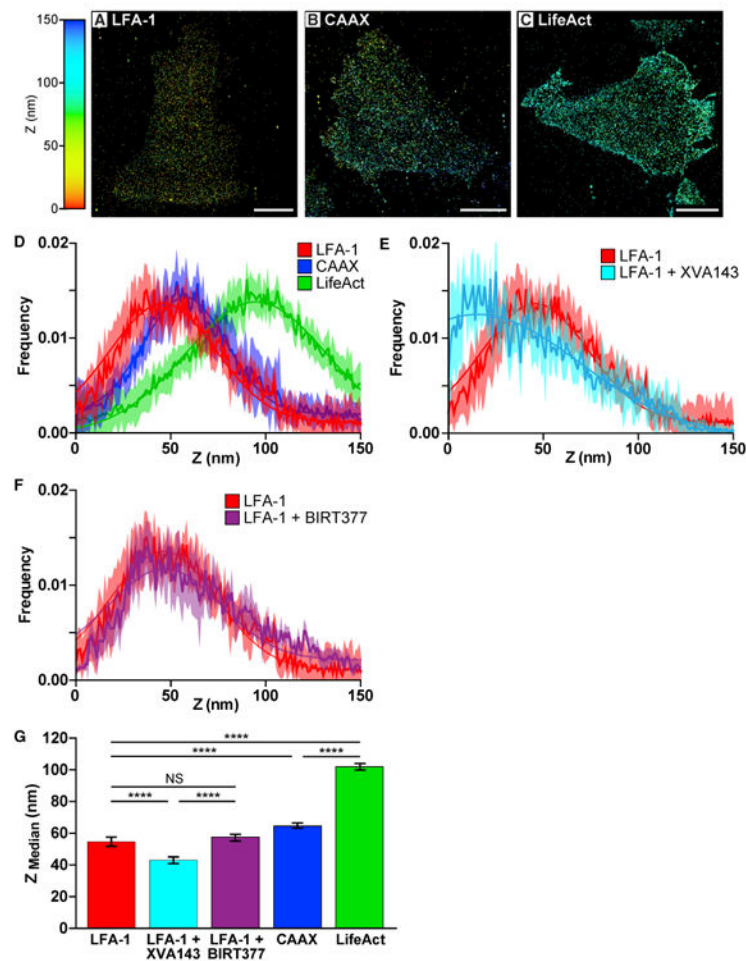
Figure 3. Localization of LFA-1 Headpiece and Effect of Small-Molecule Agonists in Cells Migrating on Fibronectin

(A–C) Representative iPALM renderings of Jurkat cells expressing mEOS3.2-LFA-1 fusion (A), mEOS3.2-CAAX (B), or LifeAct-mEos3.2 to label actin (C) migrating on coverslips coated with 10 μg/mL fibronectin. Single-molecule iPALM localizations are color-coded by Z position as shown in scale on left. Larger dots correspond to fiducial markers. Scale bars, 5 μm.

(D–F) Frequency histogram, with 1nm bins, of axially localized mEOS3.2 emissions relative to the coverslip (Z = 0) in Jurkat cells migrating on coverslips coated with 10 μg/mL fibronectin. Data are for the sum of measurements over N cells expressing mEOS3.2-LFA-1 (red, n = 12), treated with 10 μM XVA143 (cyan, n= 11), treated with or 20 μM BIRT377 (purple, n = 8), CAAX-mEOS3.2 (blue, n = 11), LifeAct-mEOS3.2 (green, n = 12). Plots show the frequency (thick line) with 95% bootstrapped confidence interval (shaded region) and Gaussian fit (thin line) of the frequency for each construct. (G) Mean Z median ± SD among n individual cells of mEOS3.2 emission axial localizations for Jurkat cells migrating on coverslips coated with 10 μg/mL fibronectin. Two-tailed Mann-Whitney tests that compared results among n individual cells enumerated in D gave p values coded as ****p < 0.0001 or not significant (NS).
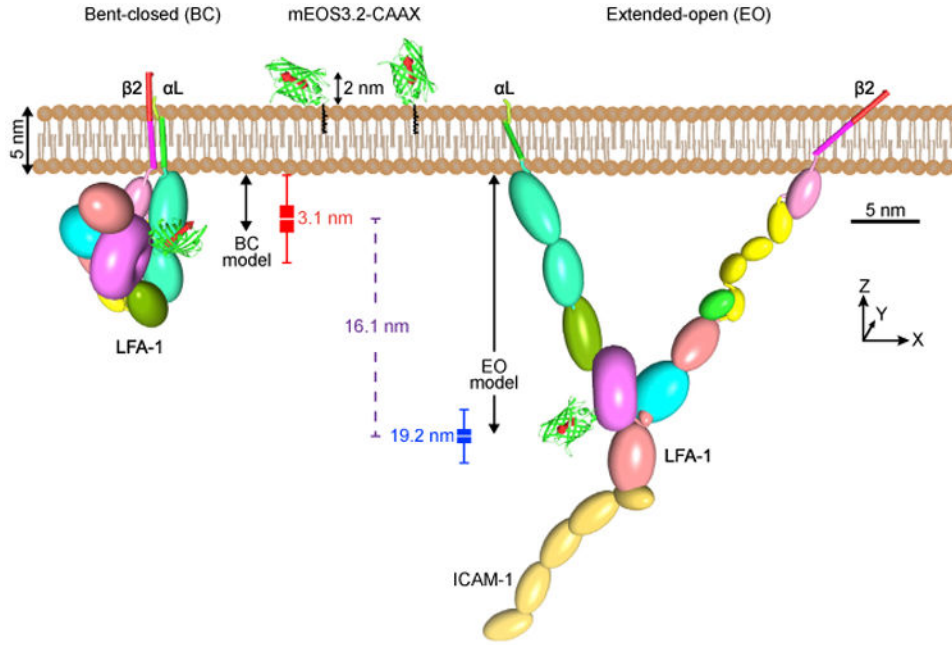
Figure 4. Comparison of Experimental Measurements to Integrin Models
Models of mEos3.2-LFA-1 show extracellular integrin and ICAM-1 domains as ellipsoids or toroids and structurally defined regions of transmembrane and cytoplasmic domains as cylinders (α-helix) or worm-like chains (coils). mEos3.2 inserted in the integrin or with a prenylated C-terminal CAAX sequence is shown as a green ribbon cartoon with a red double-ended cylindrical arrow showing fluorophore position and dipole orientation. Estimates from Table 2 of mEOS3.2-LFA-1 fluorophore height above the membrane on fibronectin and ICAM-1 substrates are shown as thick bars extending ± 1 SEM and lines extending ± 1 SD. The difference in distance between mEOS3.2-LFA-1 Z localizations on fibronectin and ICAM-1 substrates is shown as a dashed line. LFA-1 in the bent-closed conformation and in an ICAM-1-bound extended-open conformation with a tilt of 45° in a previously defined reference frame (Nordenfelt et al., 2017) are shown to scale with the height above the membrane of the mEOS3.2 fluorophore measured from atomic coordinates shown as double-ended black lines with arrowheads at each end.

Table 1

mEOS3.2 Fluorophore Z Distance Measurements

Construct	Substrate	Treatment	Z Median Average by Cell (nm)[a,e]	Z Median All Cells (nm)[b,e]	Gaussian Z Center (nm)[c,e]	R²[d]	No. Cells	No. Molecules
LFA-1-mEos3.2	ICAM-1	–	36.1 ± 1.5	36.1 ± 0.7	29.3 ± 1.0	0.97	12	1.18×10^6
LFA-1-mEos3.2	ICAM-1	Mn^{2+}	32.0 ± 1.9	32.0 ± 0.7	25.5 ± 1.2	0.95	9	8.23×10^5
CAAX-mEos3.2	ICAM-1	–	62.3 ± 1.4	61.0 ± 0.7	55.7 ± 0.9	0.92	13	1.07×10^6
LifeAct-mEos3.2	ICAM-1	–	95.3 ± 1.3	94.9 ± 0.5	95.7 ± 0.7	0.98	10	1.48×10^6
LFA-1-mEos3.2	fibronectin	–	50.9 ± 2.9	50.1 ± 0.7	45.8 ± 4.1	0.95	12	1.04×10^6
LFA-1-mEos3.2	fibronectin	XVA143	40.4 ± 2.0	40.8 ± 1.0	15.4 ± 1.4	0.92	11	6.78×10^5
LFA-1-mEos3.2	fibronectin	BIRT377	53.3 ± 2.0	54.2 ± 0.9	46.6 ± 1.1	0.87	8	4.69×10^5
CAAX-mEos3.2	fibronectin	–	61.0 ± 1.8	61.3 ± 0.6	57.5 ± 1.5	0.97	11	1.02×10^6
LifeAct-mEos3.2	fibronectin	–	95.6 ± 2.1	96.6 ± 0.5	94.9 ± 2.5	0.98	12	3.55×10^6

[a] Average of Z medians for each cell $\pm$ SD.

[b] Z median of combined localizations $\pm$ bootstrapped 95% confidence interval.

[c] Average of Gaussian Z centers for each cell $\pm$ SD.

[d] R^2 value for Gaussian Z center fits for combined localizations; the corresponding fit curves are shown in figures.

[e] All measurements relative to the coverslip ($Z = 0$).

Table 2

LFA-1 Fluorophore Distance from CAAX Fluorophore and Estimate of LFA-1 Fluorophore Height above Membrane

Construct	Substrate	Treatment	Difference from CAAX (nm)[a]	Height Estimate from Membrane (nm)[b]
LFA-1-mEos3.2	ICAM-1	–	26.2 ± 2.0	19.2 ± 2.0
LFA-1-mEos3.2	ICAM-1	Mn^{2+}	30.3 ± 2.3	23.3 ± 2.3
LFA-1-mEos3.2	fibronectin	–	10.1 ± 3.4	3.1 ± 3.4
LFA-1-mEos3.2	fibronectin	XVA143	20.6 ± 2.7	13.6 ± 2.7
LFA-1-mEos3.2	fibronectin	BIRT377	7.7 ± 2.7	0.7 ± 2.7

[a] Difference between Z median of LFA-1 fluorophore and mEos3.2-CAAX on same substrate ± error-propagated SD.

[b] Estimate of LFA-1 fluorophore height above the extracellular face of the membrane bilayer ± error propagated SD (difference from CAXX with subtraction of 5 nm membrane thickness and 2 nm estimated distance of mEos3.2-CAAX fluorophore from the inner leaflet of the membrane).